ADVANCED MATERIALS TECHNOLOGIES
www.advmattechnol.de

A Facile Approach for 4D Microprinting of Multi-Photoresponsive Actuators

*Li-Yun Hsu, Philipp Mainik, Alexander Münchinger, Sebastian Lindenthal, Tobias Spratte, Alexander Welle, Jana Zaumseil, Christine Selhuber-Unkel, Martin Wegener, and Eva Blasco**

For microscale 4D photoresponsive actuators, light is crucial in two ways. First, the underlying additive manufacturing techniques rely on photopolymerization processes triggered by the absorption of light. Second, the absorption of light serves as the actuation stimulus. The two absorptions can be conflicting. While the microstructure requires strong absorption at the actuation wavelength(s), this absorption should not interfere with that of the manufacturing process. Herein, a simple strategy is proposed to overcome these limitations and allow for the fabrication of multi-photoresponsive 3D microstructures that can be actuated at different wavelengths of light. Two-photon 3D laser printing is selected as the fabrication technique and liquid crystalline (LC) elastomers as the functional materials. In a first step, 3D microstructures are fabricated using an aligned LC ink formulation. Thereafter, up to five different dyes exhibiting absorptions that extend over the entire visible regime (400–700 nm) are successfully incorporated into the LC microstructures by an exchange process enabling a programmable actuation by irradiating with the suitable wavelength. Furthermore, by combining dyes exhibiting orthogonal absorptions, wavelength-selective actuations are demonstrated.

1. Introduction

Additive manufacturing, also known as 3D printing or direct laser writing, has become a widespread tool thanks to its ability to produce complex geometries on the micrometer scale that may be difficult or impossible to manufacture by other means.[1] Among all the available additive manufacturing technologies, light-based 3D printing is highly attractive.[2] In particular, 3D laser printing relying on two-photon polymerization processes has been established as a powerful methodology for micro- and nano-meter-scale 3D fabrication.[3] In addition, within the last few years, major efforts have also been made in the development of new approaches enabling, for example, faster and more economical 3D printing and/or higher resolution.[4]

Along with the development of new 3D laser printing technologies, the implementation of functionality in the printable materials opens the door to real-life applications.[5] In particular, the ability to change the properties of a 3D printed object versus time in a controlled fashion upon response to an external stimulus opens new possibilities in different fields, including (micro) robotics or biomedical applications.[6] This concept is frequently referred to as "4D printing", where time serves as the fourth dimension.[7] In the past few years, stimuli-responsive materials, especially hydrogels,[8] shape memory polymers (SMPs),[9] composites,[10] and liquid crystalline (LC) elastomers,[7a,11] have been most intensively explored in the

L.-Y. Hsu, P. Mainik, E. Blasco
Organic Chemistry Institute
Heidelberg University
69120 Heidelberg, Germany
E-mail: eva.blasco@oci.uni-heidelberg.de

L.-Y. Hsu, P. Mainik, E. Blasco
Centre for Advanced Materials
Heidelberg University
69120 Heidelberg, Germany

A. Münchinger, M. Wegener
Institute of Applied Physics
Karlsruhe Institute of Technology (KIT)
76128 Karlsruhe, Germany

The ORCID identification number(s) for the author(s) of this article can be found under https://doi.org/10.1002/admt.202200801.

DOI: 10.1002/admt.202200801

S. Lindenthal, J. Zaumseil
Institute for Physical Chemistry
Heidelberg University
69120 Heidelberg, Germany

T. Spratte, C. Selhuber-Unkel
Institute for Molecular Systems and Engineering and Advanced Materials (IMSEAM)
Heidelberg University
69120 Heidelberg, Germany

A. Welle
Institute of Functional Interfaces (IFG) and Karlsruhe Nano Micro Facility (KNMFi)
Karlsruhe Institute of Technology (KIT)
76344 Eggenstein-Leopoldshafen, Germany

M. Wegener, E. Blasco
Institute of Nanotechnology (INT)
Karlsruhe Institute of Technology (KIT)
76344 Eggenstein-Leopoldshafen, Germany
E-mail: eva.blasco@partner.kit.edu

field. Among all these materials, LC elastomers are particularly attractive due to the non-necessity of aqueous environment or external load. Moreover, their most remarkable property is their programmable anisotropy, which could lead to self-actuating, large-amplitude, and long-lifetime anisotropic motions upon stimulus. This makes them ideal materials for the realization of responsive structures. Recently, 3D printing of LC materials via two-photon polymerization has been successfully demonstrated for the fabrication of microscopic tuneable optical elements[12] and a variety of microactuators.[13] The actuation mechanism of these materials relies on the transition between the nematic and isotropic phases and can be induced by different stimuli, such as temperature or light.[14] Light is particularly attractive as a stimulus because it allows for both precise temporal and spatial control. One strategy to achieve light-driven actuation is the incorporation of an absorber molecule, such as an organic dye, which can convert the absorbed light into heat, inducing the thermal transition, and therefore, enabling actuation.[14] While using light-based printing technologies, the selected dye needs to fulfil the following requirements: i) strong absorption at the desired actuation wavelength but transparent at the printing wavelength; ii) compatibility with the liquid crystalline mesophase; and iii) good solubility and dispersibility in the ink formulation. Until date, azobenzene is the only suitable dye for the preparation of photoresponsive LC microactuators using two-photon 3D laser printing.[13a–c] The use of azobenzene dyes equipped with a photopolymerizable group in the LC ink, which can be incorporated into the LC network during printing via two-photon polymerization, is the approach employed in most of the reported examples (**Figure 1**, Approach I). Using this approach, several microactuators, such as microwalkers or microhands, have been successfully demonstrated using green light for stimulation. Nevertheless, this approach still remains limited in terms of the dye employed, and more importantly, in regard to the actuation wavelength. For example, applications in the biomedical field require red-shifted dyes to ensure good penetration depth in human tissue and to avoid damage.[15] In addition, systems that can be actuated on demand using different wavelengths of light will allow for more freedom in the actuation patterns.

Herein, we present a simple and versatile approach for the fabrication of photoresponsive 4D microstructures that can be actuated at different wavelengths in the visible range (Figure 1, Approach II). It consists of two main steps: First, 3D microstructures are laser printed using a LC formulation including unreactive LC molecules – without dye – avoiding incompatibilities during the printing process. In a second step, a dye (or a mixture of dyes) is incorporated into the 3D microstructure by replacing the unreactive LC molecules, which is further cured using UV light. To prove its versatility, we show the successful incorporation of five different dyes into the LC microstructures, enabling the actuation at wavelengths ranging from 400 to 650 nm. Furthermore, we demonstrate the fabrication of multi-responsive LC microactuators using combinations of dyes absorbing at different wavelengths, allowing for tuning the response on demand. We believe that this approach will create new opportunities in fields such as light-actuated microrobotics and that it can be easily adapted to incorporate further functionalities.

2. Results and Discussion

2.1. Dyes as Photoabsorbers

To enable the preparation of multi-photoresponsive structures, we selected diverse molecules (dyes) absorbing at different regions that will be later used for functionalization of the printed LC 3D microstructures. The dyes will absorb light and convert it into heat, inducing the nematic LC to isotropic phase transition, which results in actuation of the microstructures. Therefore, the absorption properties will dictate the wavelength of actuation. In this work, we specifically exploit three classes of dyes: azobenzene, Donor-Acceptor Stenhouse Adduct (DASA), and anthraquinone derivates, absorbing at different regions of the visible spectrum of light (Figure 1B).

First, two azobenzene derivatives (**Azo1** and **Azo2**) were synthesized (see details in the Supporting Information). Both azobenzenes exhibited an absorption maximum at 438 nm after being functionalized with amino- and carboxylate groups in the para position as electron–donor/acceptors. While **Azo1** was equipped with acrylate groups as photocrosslinkable units, **Azo2** carried only aliphatic chains without polymerizable groups. The purpose was twofold: i) to have a direct comparison between the conventional approach and our new approach; and ii) to investigate the role of the photopolymerizable groups in the current approach, specifically in the second post-modification step. Second, we synthesized two Donor–Acceptor Stenhouse Adducts derivatives (**DASA1** and **DASA2**) absorbing in green light regime. While the dialkylamine-based first generation **DASA1** exhibited its maximum absorption at 569 nm, substituting the electron-donating moiety into a secondary aniline led to the formation of the second generation **DASA2**, which exhibited a red-shifted absorption spectrum (Figure 1B).[16] These specific dyes were selected due to their orthogonal absorption with respect to the well-established azobenzene dyes (see Section 2.3.2).[17] It should be noted that DASA dyes have not been exploited to date as absorber units in LC networks. Furthermore, the anthraquinone derivative Sudan Blue II (**SBII**), which is commercially available, was chosen due to its absorption at longer wavelengths with an absorption maximum above 650 nm.

2.2. Fabrication and Characterization of Photoresponsive LC Microstructures

As described above, successful fabrication of light-driven LC microactuators requires the incorporation of suitable dyes into the 3D printed microstructures. Conventional approaches focus on the incorporation of the dye directly into the formulation, which drastically limits the number of choices. Here, we describe a new approach that comprises two main steps: i) alignment and 3D laser printing of a LC formulation transparent at the writing wavelength and ii) incorporation of functionality by diffusion of dyes into the 3D microstructures. The development and optimization of both steps as well as an in-depth characterization of the functionalized 3D microstructures to ensure optimal response are described in the following paragraphs.

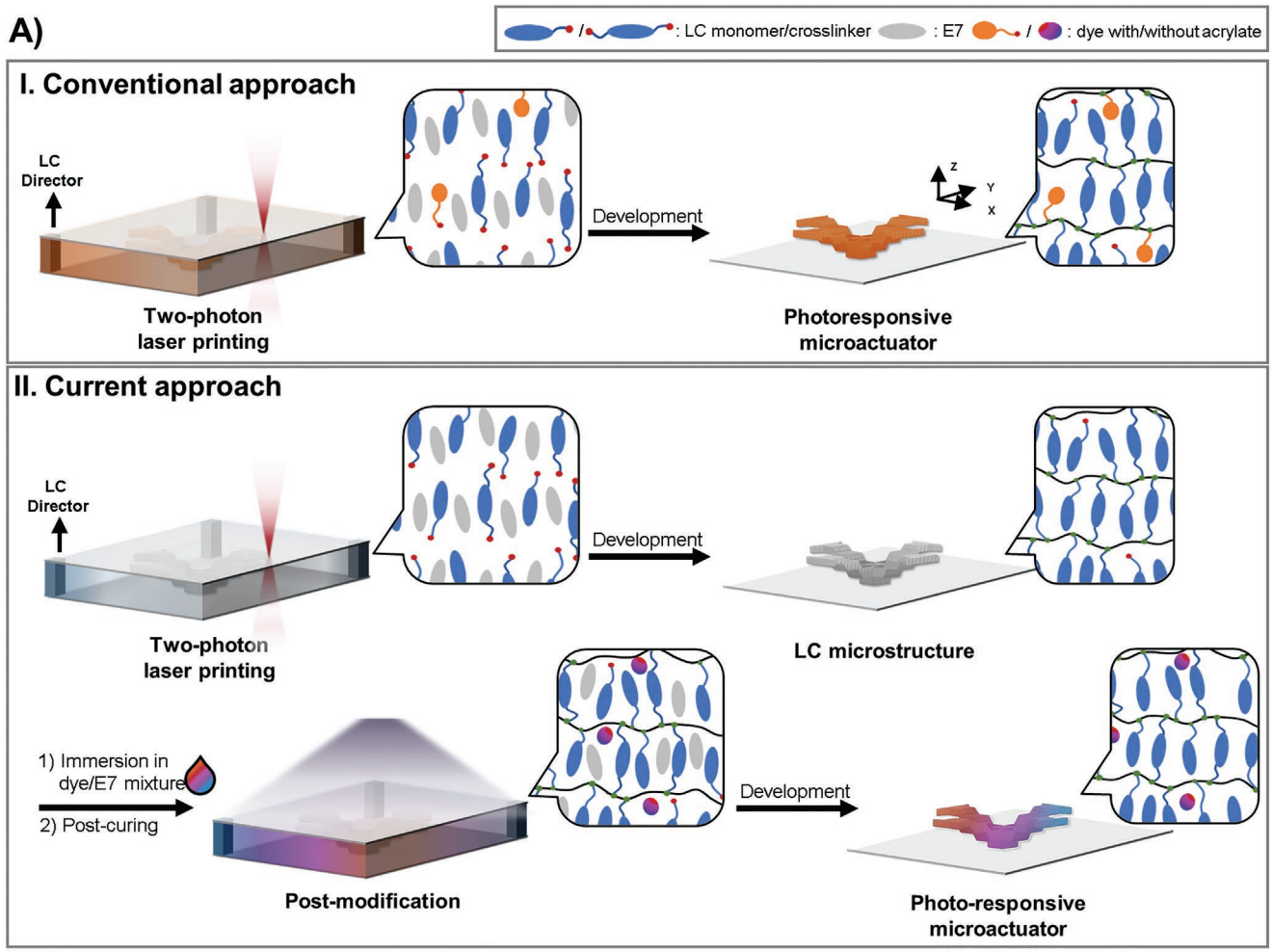

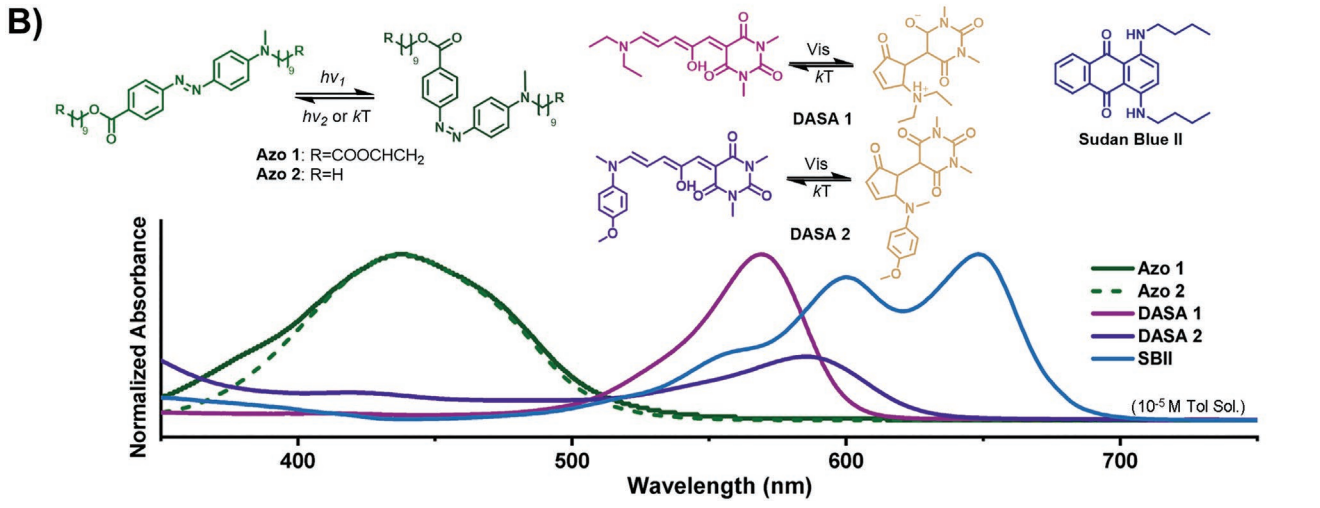

Figure 1. A) Schematic illustrations of the fabrication of photoresponsive 3D microstructures via two-photon 3D laser printing. i) Conventional approach: LC ink containing photoresponsive units is aligned in a glass cell and used for two-photon 3D laser printing. ii) Approach introduced here: first, 3D microstructures are fabricated from LC ink (without photoresponsive units) as in the previous step. After printing, the photoresponse is incorporated via diffusion using a dispersion of dye(s) in a E7 LC mixture and exposed to light for further photo-crosslinking. This approach enables the incorporation of dyes absorbing at different wavelengths or mixtures of them. B) Chemical structures and absorption spectra of the employed dyes. The UV–vis spectra were measured in solution (concentration = 10^{-5} M in toluene).

2.2.1. Alignment and Printing of the LC Ink

The employed LC formulation consisted of a mixture of three well-known LC molecules: i) acrylic monomer (**1**, 16.4 wt%); ii) bifunctional-acrylate crosslinker (**2**, 32.8 wt%); and iii) unreactive E7 mixture (**3** 49.2 wt%). To facilitate two-photon polymerization, phenylbis (2,4,6-trimethylbenzoyl) phosphine oxide (**4**, 1.2 wt%) was added as photoinitiator. In addition, butylated hydroxytoluene (**5**, 0.4 wt%), was included to increase the thermal stability, acting as a radical scavenger for improving the printing resolution (see further details in the Experimental Section). The optimization of the composition, especially the amount of E7 mixture, was very important for the success of the second step, that is, dye incorporation.

In a first step, we performed the alignment of the LC ink. This step is critical as the orientation needs to be preserved during the printing process to ensure an optimal actuation response of the 3D microstructures later. Using polymer alignment layers on the surface of the substrate is one of the most straightforward strategies and is easily adaptable to our printing setup.[18] In particular, a sandwich glass cell, whose surfaces were coated with polyimide layers enabling vertical alignment, was constructed using 30 µm spacers. The cell was then filled with the LC ink by capillary forces while heating it above the nematic-to-isotropic transition temperature (T_{ni}), which is ≈60 °C for the employed LC formulation (Figure S1, Supporting Information). After cooling down to room temperature, the LC homeotropic alignment was verified with polarized optical microscopy (POM), showing a black and monochromatic image regardless of the orientation of the sample to the crossed polarizers.[19] Thereafter, the aligned LC cells were employed for 3D laser printing using a commercial two-photon lithography setup (see Experimental Section).

The optimized LC ink formulation allowed for the use of a broad range of printing parameters (laser power and scanning speed) while maintaining good printing performance. In order to characterize the 3D printed microstructures at the different conditions in-depth, we employed confocal Raman spectroscopy. For these measurements, 3D blocks ($50 \times 50 \times 10$ µm^3) were successfully printed by varying the parameters: laser power from 22.5 to 35 mW and the scanning speed from 3 to 9 mm s^{-1}. To monitor the polymerization degree, we used the double-bond stretching band of the acrylate group at 1635 cm^{-1}. As expected, we observed a decrease in the intensity compared to the unpolymerized ink due to the consumption of double bond during printing (**Figure 2**A). Furthermore, we used this signal to calculate the double bond conversion (DOC)[20] (Equation (S1), Supporting Information). The stretching signal of the carbonyl groups C=O (1726 cm^{-1}) served as a reference peak as this group is not affected during photopolymerization. The results (Figure 2B) showed that the DOC was highly dependent on the laser dose: the higher the laser power or the slower the scanning speed, the higher the degree of polymerization. While keeping the scanning speed constant at 5 mm s^{-1} (Figure 2B, blue axis), a significant increase of the DOC from 0.68 to 0.80 was observed when the laser power was increased to 30 mW (Figure 2B, blue dashed line). Interestingly, the effect in the DOC was not so prominent for different scanning speeds at a certain laser power (red dash line). These results were in good agreement with the mechanical properties measured by nanoindentation (Figure 2C). When keeping the laser power at 27.5 mW and only changing the scanning speed from 5 to 9 mm s^{-1}, the effective Young's modulus (E_{eff}) on microblocks only varied within a small range from 15.4 to 17.6 MPa. In contrast, E_{eff} = 35.3 MPa was obtained for the blocks printed with the same scanning speed of 5 mm s^{-1} but with an increased laser power of 30 mW. We interpret this behavior as being a consequence of the higher conversion, and therefore, more densely crosslinked LC networks.

As mentioned above, the E7 mixture plays an important role. Although it is not reactive during printing, these molecules not only facilitate the alignment of the ink before fabrication by inducing a lower viscosity but also enable the formation of a network during printing that contains enough flexibility for the incorporation of the dye in a second step. Unfortunately, having a large fraction of unreactive E7 mixture during printing resulted in an unwanted and severe shrinkage (≈49%) of the 3D microstructures after development due to the washing of the unpolymerized LC ink with the E7 mixture inside the printed 3D microstructure (Figure S2, Supporting Information). However, we found that it was possible to recover partially the original shape of the 3D printed microstructure by re-immersing the developed microstructures into an E7 mixture followed by a UV light post-curing step. We assumed that the remaining acrylate groups were further polymerized and formed a more crosslinked, and therefore, more stable network. This hypothesis was corroborated by Raman spectroscopy by following the double bond band once again. As depicted in Figure 2B, an increase in the DOC was observed for all UV post-cured microstructures. For example, a 10% increase in DOC was observed for the samples printed at 27.5 mW of laser power (solid blue line).

2.2.2. Incorporation of Photoresponsive Units Into LC 3D Microstructures

Based on the previous findings, we explored the potential of using the "re-swelling" and UV curing procedure for introducing other functional molecules into the LC microstructures, such as dyes. First, we printed simple cubic blocks ($50 \times 50 \times 10$ µm^3) using the LC ink and incorporated the first family of azobenzene dyes in the second step, denoted as LC ⊃ **Azo1** and LC ⊃ **Azo2**. For that, we employed dispersions consisting of azo dyes and an E7 mixture. After the same UV curing and development steps, the incorporation of the azobenzene dyes was confirmed by Raman spectroscopy. In both cases, the spectra showed the characteristic C−N stretching signal of azobenzenes ν (C−N)$_{Azo}$ at 1137 cm^{-1}. Interestingly, **Azo2** was also retained in the LC microstructures despite not having photopolymerizable groups (Figure 2A). We assumed that after UV curing, **Azo2** was "trapped" inside the more densely crosslinked 3D microstructure via non-covalent interactions, such as π–π stacking.

The degree of functionalization of the 3D microstructures using the two azobenzene dyes was further investigated in detail using LC microstructures printed at different conditions and with varying concentrations of the dyes in the E7 mixture (5 wt% and 20 wt%) in the second step. In brief, we calculated the incorporation of the azobenzene in respect to the LC moieties in the microstructure by using the peak

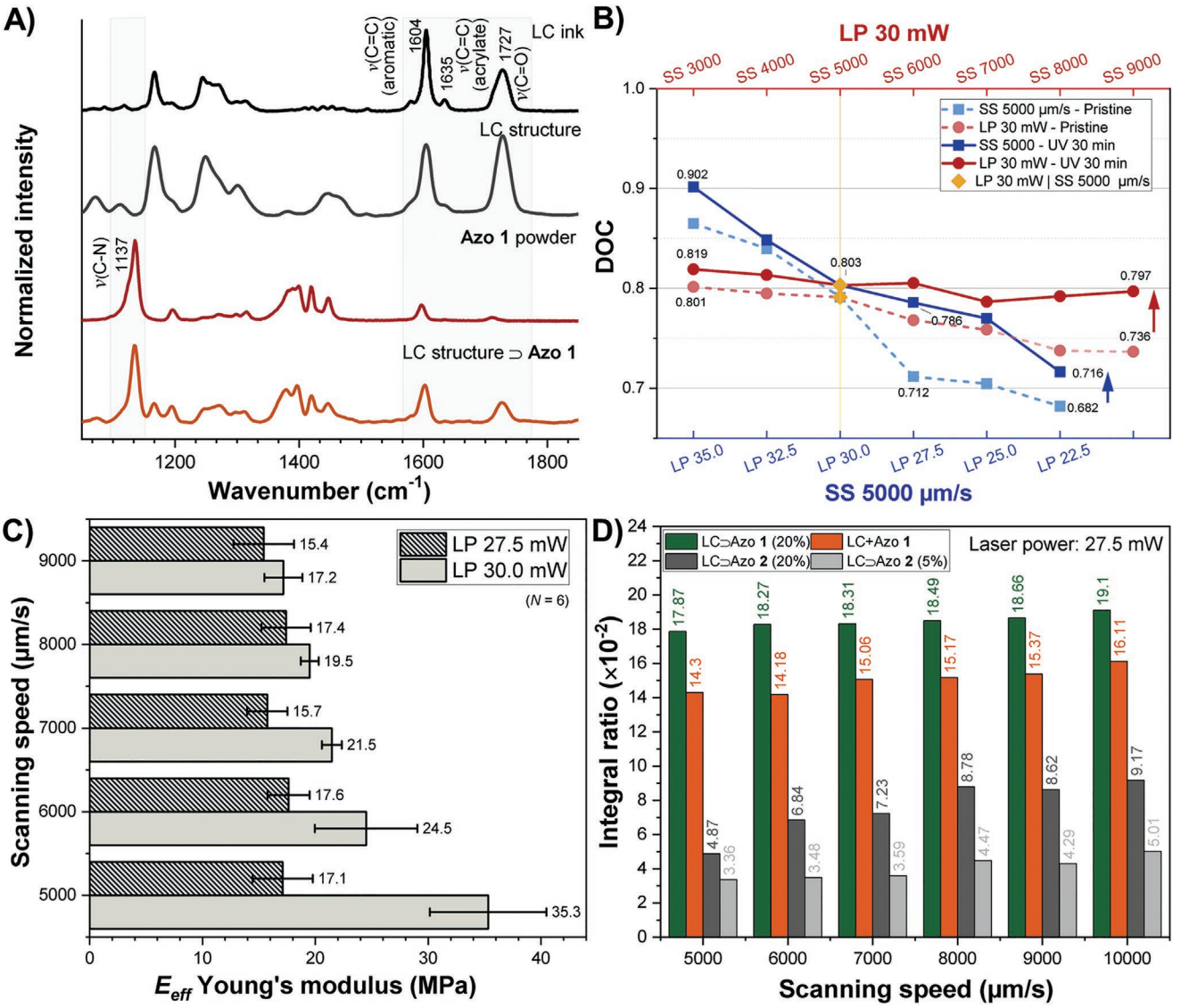

Figure 2. A) Raman spectra of the unpolymerized ink, pristine LC microstructure, pure **Azo1** powder, and LC microstructure (LC ⊃ **Azo1**). B) Calculated double bond conversion (DOC) for 3D microstructures printed under various conditions. The characteristic peaks of ν (C=O) (1727 cm^{-1}) and ν $(C{=}C)_{acrylates}$ (1635 cm^{-1}) were used for the analysis of DOC. C) Mechanical characterization of LC microstructures printed at different laser powers and scanning speeds. The error bars represent the standard deviation based on six measurements. D) Comparison of the dye integral ratio between the conventional approach (LC + **Azo1**) and the current approach (LC ⊃ **Azo1** and **Azo2**), based on the value of ν $(C=O)_{Azo}/\nu$ $(C{=}O)_{LC}$ from the Raman spectra.

areas of the corresponding signals (ν $(C{=}O)_{Azo}/\nu$ $(C{=}O)_{LC}$, see Equation (S2), Supporting Information). The first observation was that the printing conditions had an impact on the dye penetration for both azobenzenes (Figure 2D). For instance, a higher amount of dye was trapped in the 3D micrometric blocks printed with a scanning speed of 10 mm s^{-1} than the ones printed at 5 mm s^{-1}. In addition, the functionalization degree could be tuned by using different concentrations of dyes in the E7 mixture. For example, dye dispersions until 20 wt% in E7 mixture were successfully employed. Furthermore, while using the same concentration of azo dyes in the E7 mixture, a higher degree of functionalization for **Azo1** in comparison to **Azo2** was observed due to its covalent attachment to the LC polymeric network during the post-curing step.

In order to have a direct comparison with the conventional approach, we also prepared 3D cubic microstructures by directly incorporating **Azo1** and **Azo2** in the ink formulation (denoted as LC + **Azo1** and LC + **Azo2**) and analyzed by Raman spectroscopy. While the ν $(C{-}N)_{Azo}$ was detected for LC + **Azo1**, no signal was found for LC + **Azo2**, indicating that **Azo2** was washed away during the development process (Figure S3, Supporting Information). In addition, it should be noted that the concentration of dyes was limited to 2.5 wt% here. Above these concentrations, crystallization and disruption of the alignment as well as "micro-explosions" during printing were observed. Therefore, these experiments allowed us to prove the clear advantages of the new approach: i) incorporation of non-acrylate dyes, facilitating the synthesis; and ii) possibility of controlling

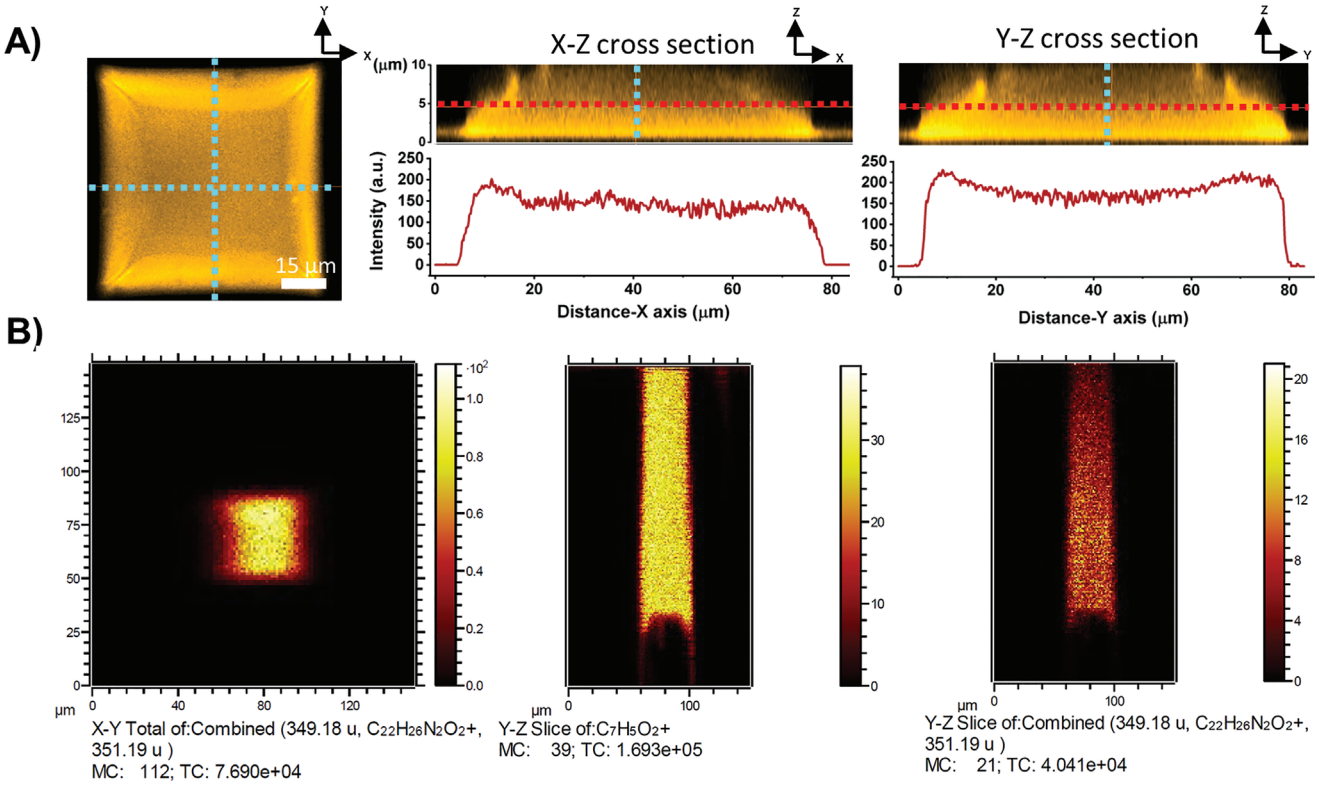

Figure 3. A) Fluorescence images of LC ⊃ **DASA1** 3D microblock ($75 \times 75 \times 10$ µm^3) acquired from confocal laser scanning microscope, displaying *X*–*Y*, *X*–*Z*, and *Y*–*Z* cross sections (slices indicated by blue dashed line). The intensity profiles were measured at the red dashed lines. B) Cross-sections of LC ⊃ **SBII** block ($40 \times 40 \times 10$ µm^3) (field of view $X = Y = 150$ µm, *Z* not to scale) from ToF-SIMS analysis. Ar_{1500} cluster depth profiling signal of $C_7H_5O_2^+$ indicates the LC polymer (middle) and $C_{22}H_{26}N_2O_2^+$ (plus isotope distribution) is characteristic for **SBII** (right, in positive secondary ion polarity).

the dye incorporation without the necessity of modifying and optimizing the printing parameters.

We also applied the established methodology for the incorporation of azo dyes to the other classes of dyes, the DASA derivatives and the anthraquinone derivative, Sudan Blue II (**SBII**). The incorporation of the dyes was first proved by optical microscopy (Figure S7, Supporting Information). Colorful 3D microstructures (magenta for LC ⊃ **DASA1**, dark violet for LC ⊃ **DASA2**, and indigo blue color for LC ⊃ **SBII**) were obtained. Importantly, the functionalization did not affect the alignment, showing DASA dyes compatibility with the LC network for the first time. In analogy to our previous results with azobenzene, it was possible to incorporate derivatives without acrylate groups. It should be noted that the synthesis of acrylate-DASA derivatives is synthetically very demanding. Furthermore, the use of the DASA dyes directly in the formulation for comparison was not possible for two reasons: i) poor miscibility of the DASA in the LC formulation and ii) instability of the DASA in the radical polymerization conditions. Thus, this is also a clear advantage of the presented approach.

Further investigations of the dye distribution within the LC microstructure after post-functionalization were performed by monitoring the fluorescence as well as the molecular mass of the DASA derivatives and **SBII** by using confocal laser scanning microscopy and time-of-flight secondary ion mass spectrometry (ToF-SIMS), respectively. As shown in **Figure 3**A, the comparable fluorescence intensity profiles of **DASA1** (λ_{em} = 595 nm) in both *X*–*Z* and *Y*–*Z* slices of a functionalized LC microblock ($75 \times 75 \times 10$ µm^3) indicated the well penetration of the dye within the structure and not only in the surfaces. These observations were consistent with the ToF-SIMS analysis (Figure 3B). For example, the m/z signal detected at 349.18 ($C_{22}H_{26}N_2O_2^+$), characteristic of **SBII** showed comparable signal intensity in the whole 3D microblock ($40 \times 40 \times 10$ µm^3). Similar results were also obtained for **DASA2** (Figure S8, Supporting Information).

2.3. Toward Complex Light-Driven LC Microactuators

2.3.1. Single-Color Light Actuation

Once we had proven the successful incorporation of the different dyes into LC microstructures, we studied the photoactuation in more complex geometries. To this end, we designed a four-arm gripper: each arm of the gripper has a length of 65 µm and ends with a broader edge at the arm tip to further facilitate image analysis during the actuation characterization. In order to maximize the printed volume within the height of the glass cell, the arms were not designed straight but "staircased" (**Figure 4**A). The fabrication process was performed in a 30 µm thick cell where the LC ink was homeotropically aligned. After the development of the printed microstructures and the dye incorporation, an up-bending deformation of the arms along the director was observed, resulting in microactuators

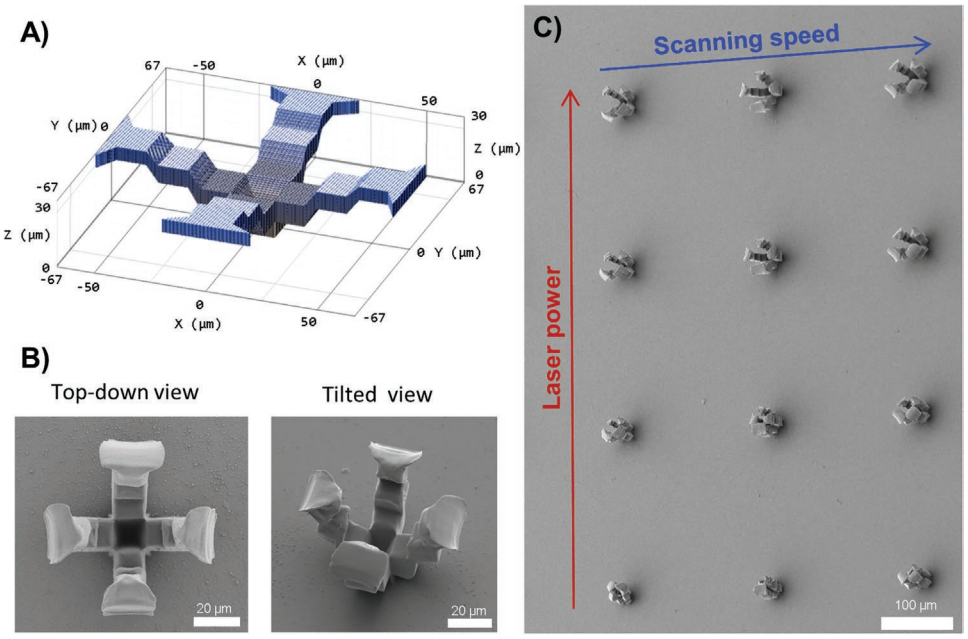

Figure 4. A) 3D model design of the microactuator. B) Scanning electron microscopic (SEM) images of LC microactuators: top view (left) and tilted view (right). C) Array of LC micro-actuators printed at different laser power (27.5–35 mW) and scanning speed (5–9 mm s^{-1}).

of a height of ≈55–65 μm (Figure 4B; Figure S9, Supporting Information). Interestingly, the shrinkage perpendicular to the alignment direction did not just lead to a shorting of the arms but also to a clear bending, inducing the actuation to its "closed state". As expected, this bending was highly dependent on the crosslinking density of the printed structures, and therefore, it could be tuned by different printing parameters (e.g., laser power and scanning speed (Figure 4C). By inducing the nematic-to-isotropic transition, it was expected that the gripper would open due to the elongation of the arms. Prior to the light-driven actuation studies, a reference sample without dye was studied to confirm the actuation pattern by temperature as a stimulus. The 3D microactuators showed the expected actuations. At 270 °C, the 3D grippers reached their maximum expansion. By cooling down to room temperature, a complete recovery to the initial state was observed (Figure S10, Supporting Information).

As a next step, five 3D microactuators, each incorporating one of the five dyes (LC ⊃ **Azo1**, **Azo2**, **DASA1**, **DASA2** or **SBII**) and one fabricated with **Azo1** using the conventional method (LC + **Azo1**) for comparison, were employed to study their photoresponse at the corresponding wavelengths of light. In order to exploit the maximum potential actuation, all structures were functionalized using highly concentrated solution of dyes (see details in the Experimental Section) to ensure that we were above the activation threshold. The actuation was monitored with a light microscope and imaged either in top or side view, while irradiating with an LED emitting at 459 nm for the 3D microactuators containing **Azo1** or **Azo2** photoabsorber (LC ⊃ **Azo1** or **Azo2**), at 520 nm for LC ⊃ **DASA1** or **DASA2**, and at 622 nm for LC ⊃ **SBII**. Under light irradiation using the suitable wavelength, an unfolding motion similar to the reference sample using temperature as stimulus was observed for all functionalized actuators (**Figure 5**A; Movie S1, Supporting Information). This was a clear indication that the absorption of the dye induces a temperature increase resulting in the thermal liquid crystal to isotropic transition. The exact temperature reached in the microstructures after irradiation is not known to us. The extent of movement could be modulated by tuning the light intensity of the LEDs. For example, as depicted in Figure 5B for a 3D gripper containing **Azo1**, the angle between the arms and the substrate gradually decreases from 51° to 10° by increasing the electrical current from $I = 0$ A, 3 A to 5A (corresponding to 1.4 to 2.0 W cm^{-2} for the blue LED).

We monitored the actuation of all the photoresponsive microactuators (Figure 5C; Figure S11, Supporting Information) over 50 cycles (on–off light) by analyzing the changes in the tip distance ΔL ($L' - L^0$) compared to the initial configuration L^0 (Figure 5B) The first noticeable difference between them was the maximum distance (L_{max}) reached (Figure 5D). Remarkably, an increase of 65% in L was achieved for LC ⊃ **Azo1**, compared to 27% for the reference LC + **Azo1**. This is the largest effect so far seen for 3D microactuators whose alignment was based on surfaces. This result emphasized the advantage of the current method in enabling the enhancement of dopant concentration (vide supra) and thus, the actuation amplitude.

Furthermore, a comparable actuation for LC ⊃ **Azo2** to the reference LC + **Azo1** was observed, despite the fact that **Azo2** does not equip with photopolymerizable groups and therefore, it is "only" non-covalently attached to the polymer network (Figure 2D). For LC ⊃ **DASA1** and **DASA2**, we observed increases in L of 11% and 22%, respectively, using irradiation at 520 nm (9.6 W cm^{-2}). It is worth mentioning that the actuation of the later LC ⊃ **DASA2** was comparable to the amplitude of the reference LC + **Azo1**, but interestingly, it shows less fatigue over 50 actuation cycles, indicating the better photostability of the system. In addition, LC ⊃ **SBII** microstructures allowed photoactuation driven by red light (622 nm, 3.5 W cm^{-2}),

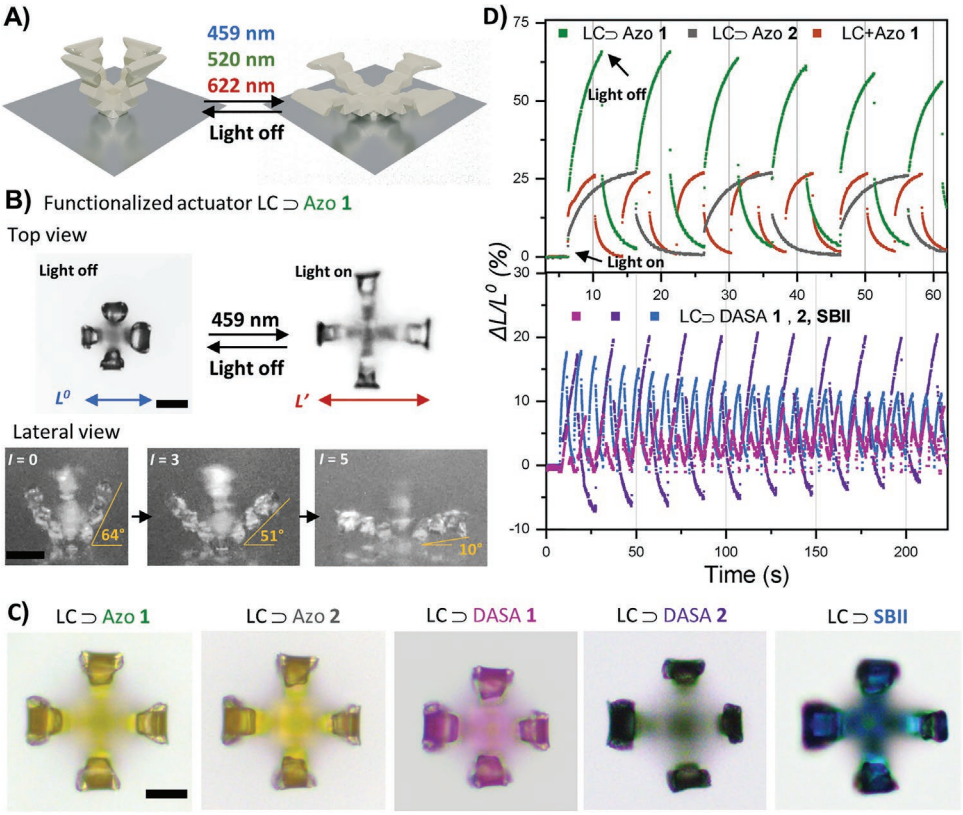

Figure 5. A) 3D representation of the reversible actuation of the 3D printed microstructures. B) Optical images showing the photoactuation of LC ⊃ **Azo1** from the top view (top row) and side view (bottom). The bending degree depended on the light intensity of the irradiated light, which was tuned by the electronic current from $I = 3$ A to 5 A. C) Optical microscope images of the printed microactuators functionalized with the different dyes: LC ⊃ **Azo1/2**, **DASA1/2**, and **SBII**. D) Response of the photoresponsive actuators by switching the light on and off, determined by the lateral expansion (%) from the top view (see the complete 50 cycles in the Supporting Information). The red, green, and blue LEDs were all set at $I = 10$ A (corresponding to 3.5, 9.6, and 3.1 W cm^{-2}, respectively) for the LC ⊃ **Azo1/2**, **DASA1/2**, and **SBII** microactuators, respectively. The scale bars are 25 µm for all microscopic images.

showing an increase in L of 18%. Importantly, these new light-driven microactuators incorporating DASAs and **SBII** dyes enable responsive structures in a new regime of the visible spectrum for actuation (see next section). In terms of temporal response (see details in the Experimental Section), the fastest actuation was observed for the azobenzene-containing microactuators: 35 ms for LC ⊃ **Azo1**, and 70 ms for LC ⊃ **Azo2** and LC + **Azo1** at the specified irradiations conditions. Temporal responses of 400–500 ms were determined for LC ⊃ **DASA2** and **SBII**, and the slowest response of ≈1 s was measured for LC ⊃ **DASA1**.

2.3.2. Multiple-Color Light Actuation

By taking advantage of the developed fabrication approach, we ultimately targeted the possibility of fabricating 3D complex microactuators, enabling more complex responses. For that, we combined two of the described dyes, which could be selectively activated by different wavelengths of light. In particular, we chose combinations of two dyes that exhibit distinct absorption regions (i.e., **Azo1** and **DASA2** or **Azo1** and **SBII**) to enable selectivity and incorporate them into the 3D printed microstructures by mixing them in the post-functionalization step. Afterward, the actuation of the dual-functionalized structures was investigated by using two LEDs emitting at different wavelengths (459 and 520 nm for **Azo1** + **DASA2**, and 459 and 622 nm for **Azo1** + **SBII**). As a reference, mono-functionalized microstructures were irradiated under the same conditions. The dual-functionalized microactuators (LC ⊃ **Azo1** + **DASA2** and LC ⊃ **Azo1** + **SBII**) showed a wavelength selective response (**Figure 6**). For instance, when only the green light was switched on, LC ⊃ **Azo1** + **DASA2** showed "half expansion" with an amplitude of 84.8%, similar to the monofunctional LC ⊃ **DASA2**, defined by the changed distance(Δd) of two opposing tips from the side view compared to the initial state (d^0) (Figure 6A). Alternatively, by only switching on the blue light, a full expansion of the bifunctional microactuator due to the activation of **Azo1** was observed, while the reference sample LC ⊃ **DASA2** did not actuate as **DASA2** only showed low absorption at 459 nm. (see Figure 6A; Movie S2, Supporting Information). We also compared the bifunctional LC ⊃ **Azo1** + **SBII** and the monofunctional LC ⊃ **SBII** (Figure 6B): while selective actuation was observed for the bifunctional microactuator by irradiating with blue light (459 nm) (Movie S3, Supporting Information), the actuation of both was possible using red light

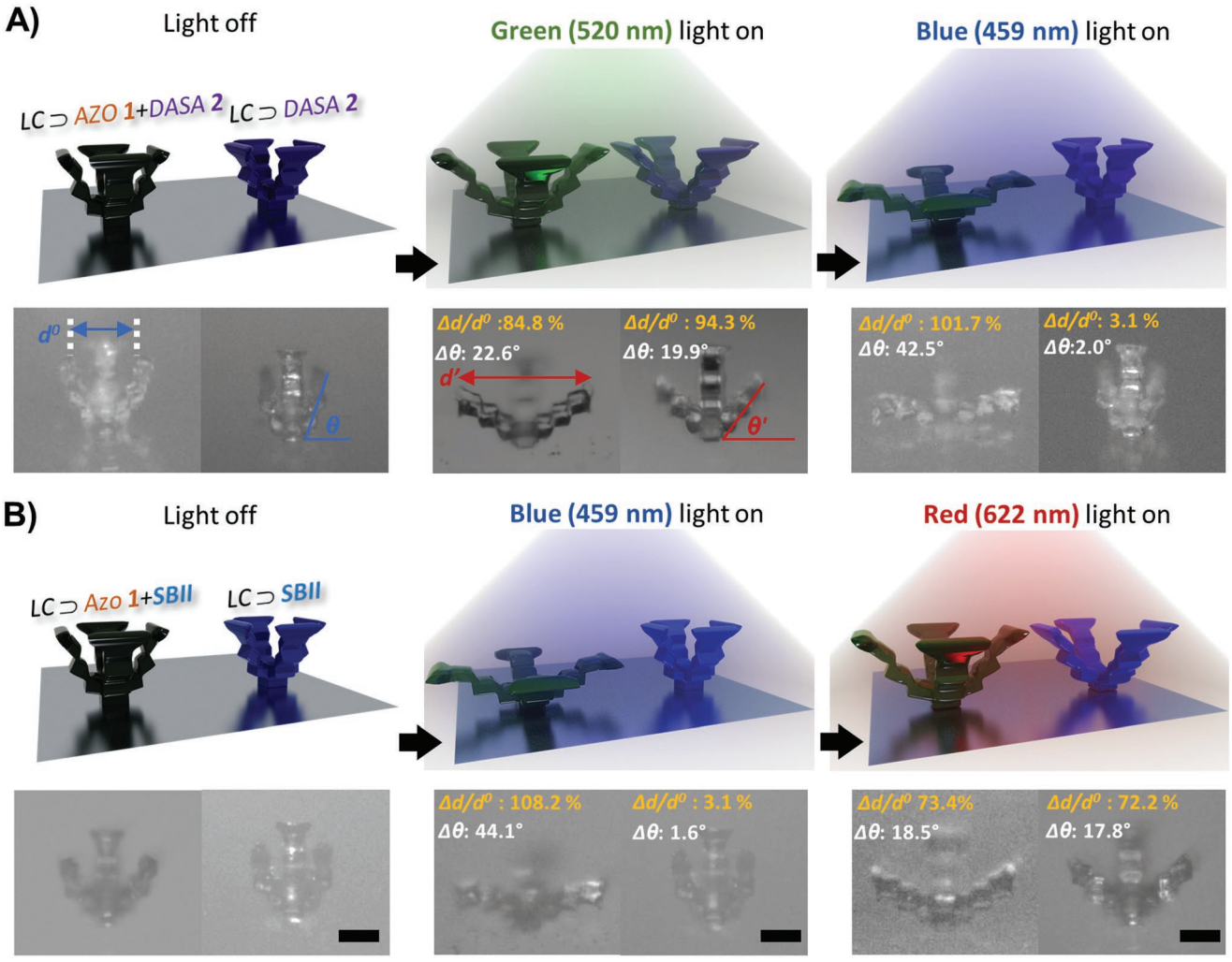

Figure 6. Wavelength-selective actuations of LC microstructures. A) LC ⊃ **Azo1** + **DASA2** and LC ⊃ **DASA2**. B) LC ⊃ **Azo1** + **SBII** and LC ⊃ **SBII** are depicted as 3D model (top) and microscope images (down). The lateral expansion and bending angle differences from the pristine state (light off) to the actuated state (red/green/blue light on) were measured ($N = 3$) from the side view for each actuated state. Scale bar = 25 µm.

(622 nm) due to the absorption of **SBII**, which was included in both. These results demonstrated that the wavelength plays a critical role in the actuation, which depends on the absorption of the dye(s) at the irradiation conditions. To the best of our knowledge, this is the first reported LC microsystem showing selective response at different wavelengths.

3. Conclusions and Outlook

We have presented a facile approach for the fabrication of multi-photoresponsive 3D microstructures using two-photon 3D laser printing as a manufacturing technique. To enable the light response, we selected different dyes: two azobenzenes, two DASAs, as well as Sudan Blue II, which all absorb in different regions of the visible spectrum. In particular, the fabrication strategy included two major steps: i) 3D laser printing of a LC formulation (transparent at the writing wavelength) and ii) incorporation of the functionalities into the printed 3D microstructure via diffusion of the corresponding dye(s) dispersed in E7 mixture. The processes were optimized to ensure optimal performance and the 3D printed microstructures were characterized in-depth. It was shown that all the 3D microstructures showed actuation under irradiation with a suitable wavelength (blue 459 nm, green 520 nm, and red 622 nm). Importantly, the versatility and performance of the fabricated microstructures were proven to be superior in comparison to the conventional "one-step" approach. The possibility of including new dyes enabling actuation at different wavelengths – in particular in the red-shifted region of the visible spectrum– and the simplicity of using dyes without further structural modification are the main advantages encountered. Furthermore, we demonstrated the realization of wavelength selective microactuators by combining two dyes exhibiting orthogonal absorption. In the near future, further efforts will be made for the fabrication of multi-material microstructures enabling wavelength-dependent and complex motions. We believe that this work opens new avenues for the facile implementation of complex functionalities in 3D printed structures that can be potentially applied to other printing techniques ranging from the micro to the macroscale,

paving the way toward the precise fabrication of multi-responsive 3D actuators with great potential, for example, in the field of smart robotics.

4. Experimental Section

Chemicals and Materials: 4-Methoxybenzoic acid 4-(6-acryloyloxyhexyloxy) phenyl ester (1), 1,4-Bis[4-(3-acryloyloxypropyloxy) benzoyloxy]-2-methylbenzene (**2**), and E7 mixture (**3**), were purchased from SYNTHON Chemicals GmbH & Co. KG. Other chemicals and solvents were supplied from either Sigma–Aldrich or Fisher Scientific unless otherwise mentioned. All materials were used as received without further purification.

Synthesis and Structure Characterization: The synthetic details are provided in the Supporting Information. All synthesized compounds were purified with flash column chromatography (Interchim PuriFlash XS520Plus) and characterized with $^{1}H/^{13}C$ nuclear magnetic resonance (NMR) spectroscopy (Bruker Avance III 400 or Bruker Avance III 300) and mass spectrometry (Bruker AutoFlex Speed time-of-flight for MALDI-MS, or Bruker ApexQe hybrid 9.4 T FT-ICR for ESI-MS). Absorption spectra were measured with a UV–vis spectrometer (Jasco V-770 Spectrophotometer) by using a 10 mm cuvette and the concentration was controlled to reach the absorbance ≈1 (10^{-5} M in toluene).

LC Ink Preparation: The LC ink was adapted from previously reported formulation.[10f] A mixture of three nematic mesogens was employed: **1**(16.4 wt%), **2** (32.8 wt%), and **3** (49.2 wt%). A photoinitiator, phenylbis (2,4,6-trimethylbenzoyl) phosphine oxide (1.2 wt%), was added in addition, to facilitate multi-photon polymerization. Besides, a radical inhibitor, 3,5-di-tert-4-butylhydroxytoluene (0.4 wt%), was included to increase the thermal stability and act as radical scavenger for improving the printing resolution. All components were first dissolved in dichloromethane and then mixed evenly by continuously stirring at elevated temperature (80 °C) under nitrogen flow until complete removal of the solvent. For fabricating **Azo1/Azo2** functionalized LC structures via conventional method, the pristine LC ink was modified by adding additional 2.5 wt% of the corresponding azobenzene powder to it and then mixing them homogeneously with the same procedure. The phase transition temperature was measured by differential scanning calorimetry (Discovery DSC 250).

Cell Construction: The cells were assembled based on previously reported methods.[8,10b,d] First, microscope cover glasses ($22 \times 22\,mm^2$, thickness $170 \pm 5\,\mu m$, Marienfeld) were cleaned by sequential sonication in acetone and 2-propanol (10 min each) and then treated with ozone-plasma cleaner (Harrick Plasma). 100 µL of polyimide (Nissan SUNEVER SE-5661) was soon after spin-coated on the glass surfaces, followed by prebaking at 80 °C for 2 min and then post-baked at 220 °C for 150 min. The cells were assembled by gluing two coverslips at the coated side together with 30 µm spacers.

Two-Photon Laser Writing of LC Microstructures: The alignment of the LC ink was achieved by filling the alignment cell with the filtered LC ink by capillary force at 80 °C followed by cooling to room temperature in a controlled manner (10 °C min^{-1}). The homeotropic alignment within the cell was confirmed by an optical microscope (Leica DM2700 M equipped with FLEXACAM C1 microscope camera) with the cell located between crossed polarizers. With the predefined orientation of the LC, two-photon laser writing was performed within a commercially available direct laser writing setup (Photonic Professional GT2, Nanoscribe GmbH & Co. KG) in oil immersion configuration with a femtosecond laser ($\lambda = 780\,nm$) focused by a 63× oil objective (NA = 1.4; WD = 190 µm; Zeiss) at the interface between the LC ink and the bottom glass. After printing, the cell was cut open and followed by development in warm 2-propanol (60 °C) for 5 min to remove unpolymerized ink. The printed microstructures were subsequently dried with mild nitrogen flow and then used for the next step for pos-modification.

Post-Functionalization of Photoresponsive Dyes Incorporation: First, the 20 wt% dye dispersions were prepared by dissolving 20 mg of the dye and 80 mg of E7 mixture in dichloromethane (1 mL), followed by solvent evaporation during stirring. The dispersions with concentration 5 wt% were prepared with the similar procedure. Next, the precipitates in the dispersion were removed with a syringe filter and then subsequently filled the gap of a new glass cell, which was assembled with an uncoated coverslip and the previously printed substrate. The immersed LC structures were kept in the dark in ambient temperature overnight and then irradiated with a UV light (380–390 nm, 14.5 mW cm^{-2}) for 30 min. Last, the excess dye mixture was removed with the same development method mentioned above and the functionalized-microstructures were prepared for further characterizations.

Characterization of the Thermoactuation: The LC microstructure was printed with a laser power of 32.5 mW and scanning speed of 5 mm s^{-1} by using the method mentioned above. The thermal actuation of it was performed in a heating stage (LTS 420, Linkam Scientific Instruments) coupled to the optical microscope. The expansion and recovery of the microactuators were induced with a programed heating cycle, heating from ambient temperature to 270 °C with a rate of 10 °C min^{-1}. At 270 °C, the temperature was kept for 5 min, followed by cooling to ambient temperature with the same rate. The distance between two opposing arm tips at the *X* and *Y* directions were tracked and averaged to obtain a mean deformation as a function of time.

Characterization of the Photoactuation: The LC microstructures were printed with a laser power of 32.5 mW and scanning speed of 5 mm s^{-1}, thereafter functionalized with each organic dye by using the method mentioned above. The functionalized LC microstructures were mounted 5 mm above the LEDs which were attached to a high precision stage. A microscope equipped with a monochrome camera (EO-5310) and a 10× objective (NA = 0.25) was used to image the samples from either top view or tilted view (30–45°) by recording with a frame rate of 28.6 fps. The LED was switched on by applying an electric current of I = 10A (corresponding to light intensities of 3.5, 9.6, and 3.1 mW cm^{-2} for red, green, and blue LEDs, respectively). Either 10 (for LC ⊃ **Azo2** and LC ⊃ **DASA2**) or 5 s (for the others) of interval was programmed for each on–off cycle, depending on the temporal response of the functionalized structures. For the comparison of the functionalized actuators, 50 continuous actuation cycles were performed (Figure S11, Supporting Information) and recorded from the top view. The amplitude *L* of each actuation cycle was defined by the mean of the distance measurements for two opposing arm tips at the *X* and *Y* directions. The measurements were performed frame by frame via ImageJ by applying an intensity threshold to improve the accuracy. The temporal response was defined as the time required to reach 50% of recovery after the light switched off ($t_{1/2}$) to compare the different microactuators using the highest light intensity.

Scanning Electron Microscopy: All scanning electron microscopic images were acquired using a Zeiss Supra 55VP (Carl Zeiss AG) at 5 kV in secondary electron mode. Prior to imaging, the structures were sputter coated with a Pt–Pd layer of 10 nm.

Confocal Raman Spectroscopy: Raman spectra were collected with a confocal Raman spectrometer (Renishaw InVia Reflex) in backscattering configuration equipped with a 633 nm laser and a 50× long working distance objective (Olympus, NA = 0.5). A calibration with a silicon wafer at 520.6 cm^{-1} was performed prior to each measurement. Each spectrum was recorded with 10 s of integration time, two accumulations, and an excitation density of 2.04 mW cm^{-2}. For the measurements of LC microstructures, blocks with dimension $50 \times 50 \times 10\,\mu m^3$ were printed and the measurements were performed at the center of the block with a focus point centered 1 µm below the surface to exclude an influence of surface inhomogeneities. To minimize the influence of spot-to-spot variations, 100 spectra were recorded over a $10 \times 10\,\mu m^2$ area of the sample and averaged after that. Spectra were fitted with Voigt functions after baseline correction and normalization at the peak maximum of ν (C=O) (1728 cm^{-1}).

Mechanical Characterization: To characterize the mechanical properties of the printed structures, glass substrates printed with blocks

dimension $100 \times 100 \times 10\ \mu m^3$ were glued to a 6-well plate and immersed in deionized water to avoid displacement during the measurements. The well plate was placed in a fiber optics-based nanoindenter (Pavone, Optics11, Netherlands) and the indentations were carried out with an indenter probe, which had a cantilever spring constant of $k = 3.57\ N\ m^{-1}$ and a spherical glass tip of 3.0 µm radius. The indentation profile was optimized with the 15 µN indentation load, a speed of $4\ \mu N\ s^{-1}$, and a hold time of 2 s before the retraction. For each microblock, indentations were repeated for eight times at different locations within the central area ($20 \times 20\ \mu m^2$) of the block. The indentation curves were analyzed with the Data Viewer (V2.5.0) software supplied by the device manufacturer to determine the Young's modulus. For this, curve fitting with a Hertzain contact model was applied in the range between the contact point (0 nm) and 150 nm.

Confocal Laser Scanning Microscopy: Fluorescence images were acquired from Nikon A1R confocal microscope (20×, NA = 0.75) equipped with GaAsP-detectors by exciting the incorporated dye molecule with 561 nm laser and detecting the fluorescence at 595 nm.

Time-of-Flight Secondary Ion Mass Spectrometry: ToF-SIMS was performed on a TOF.SIMS5 instrument (ION-TOF GmbH, Münster, Germany). This spectrometer is equipped with a Bi cluster primary ion source and a reflectron type time-of-flight analyzer. UHV base pressure was $<2 \times 10^{-8}$ mbar. For high mass resolution, the Bi source was operated in "high current bunched" mode providing short Bi_3^+ primary ion pulses at 25 keV energy, a lateral resolution of ≈4 µm, and a target current of 0.35 pA. The short pulse length of 1 ns allowed for high mass resolution. For reference measurements of the dyes, ion doses were kept below 2×10^{11} ions cm^{-2} (static SIMS limit). For charge compensation, an electron flood gun providing electrons of 21 eV was applied and the secondary ion reflectron tuned accordingly. Spectra were calibrated on the omnipresent C^-, C_2^-, and C_3^-, or on the C^+, CH^+, CH_2^+, and CH_3^+ peaks. For depth profiling, a dual beam analysis was performed in non-interlaced mode: The primary ion source was again operated in "high current bunched" mode with a scanned area of $150 \times 150\ \mu m^2$ (three frames with 128×128 data points, 125 µs cycle time) and a sputter gun (operated with Ar_{1500}^+ ions, 10 keV, scanned over a concentric field of $250 \times 250\ \mu m^2$, target current 5–5.3 nA) was applied to erode the sample for 4 s followed by a 1 s pause until the underlying glass was reached. Cross-sections were presented as recorded. For 3D representation, a 3D correction based on the flat underlying glass slide based on the Si^+ signal was performed. Software: ION-TOF Surfacelab 7.2.129059. Metadata of the TOF-SIMS experiments (doi:10.35097/605) are publicly accessible via RADAR4KIT (https://radar.kit.edu/).

Supporting Information

Supporting Information is available from the Wiley Online Library or from the author.

Acknowledgements

The authors acknowledge the funding from the Deutsche Forschungsgemeinschaft (DFG, German Research Foundation) via the Excellence Cluster "3D Matter Made to Order" (EXC-2082/1-390761711) and the Carl Zeiss Foundation through the Carl-Zeiss-Foundation-Focus@HEiKA. M.W. and E.B. acknowledge support by the Helmholtz program Materials Systems Engineering. T.S. and C.S. were supported by the German Research Foundation, project SE 1801/4-1, within the Priority Programme SPP 2206 "KOMMMA", C.S. also acknowledges the European Research Council through the Consolidator Grant PHOTOMECH (no. 101001797). The authors thank Prof. Schröder for the access to the SEM facilities and B. Weidinger and C. Vazquez Martel (Heidelberg University) for the help with the imaging. The authors also acknowledge access to the Nikon Imaging Center at Heidelberg University.

Open access funding enabled and organized by Projekt DEAL.

Conflict of Interest

The authors declare no conflict of interest.

Data Availability Statement

The data that support the findings of this study are available from the corresponding author upon reasonable request. Experimental data are publicly available via the open-access heiDATA repository (https://doi.org/10.11588/data/MR5H4A).

Keywords

4D microprinting, liquid crystal elastomers, photo-switches, stimuli responsive polymers, two-photon laser printing

Received: May 17, 2022
Revised: July 28, 2022
Published online:

[1] S. C. Ligon, R. Liska, J. Stampfl, M. Gurr, R. Mülhaupt, *Chem. Rev.* **2017**, *117*, 10212.

[2] a) Y. Yang, X. Song, X. Li, Z. Chen, C. Zhou, Q. Zhou, Y. Chen, *Adv. Mater.* **2018**, *30*, 1706539; b) J. Del Barrio, C. Sánchez-Somolinos, *Adv. Opt. Mater.* **2019**, *7*, 1900598.

[3] a) P. Kiefer, V. Hahn, M. Nardi, L. Yang, E. Blasco, C. Barner-Kowollik, M. Wegener, *Adv. Opt. Mater.* **2020**, *8*, 2000895; b) S. Maruo, O. Nakamura, S. Kawata, *Opt. Lett.* **1997**, *22*, 132; c) S. K. Saha, D. Wang, V. H. Nguyen, Y. Chang, J. S. Oakdale, S.-C. Chen, *Science* **2019**, *366*, 105; d) L. Zheng, K. Kurselis, A. El-Tamer, U. Hinze, C. Reinhardt, L. Overmeyer, B. Chichkov, *Nanoscale Res. Lett.* **2019**, *14*, 134.

[4] a) V. Hahn, T. Messer, N. M. Bojanowski, E. R. Curticean, I. Wacker, R. R. Schröder, E. Blasco, M. Wegener, *Nat. Photonics* **2021**, *15*, 932; b) M. Regehly, Y. Garmshausen, M. Reuter, N. F. König, E. Israel, D. P. Kelly, C.-Y. Chou, K. Koch, B. Asfari, S. Hecht, *Nature* **2020**, *588*, 620; c) B. E. Kelly, I. Bhattacharya, H. Heidari, M. Shusteff, C. M. Spadaccini, H. K. Taylor, *Science* **2019**, *363*, 1075; d) D. Loterie, P. Delrot, C. Moser, *Nat. Commun.* **2020**, *11*, 852; e) Q. Geng, D. Wang, P. Chen, S.-C. Chen, *Nat. Commun.* **2019**, *10*, 2179; f) V. Hahn, F. Mayer, M. Thiel, M. Wegener, *Opt. Photonics News* **2019**, *30*, 28.

[5] M. Carlotti, V. Mattoli, *Small* **2019**, *15*, 1902687.

[6] a) G. Adam, A. Benouhiba, K. Rabenorosoa, C. Clévy, D. J. Cappelleri, *Adv. Intell. Syst.* **2021**, *3*, 2000216; b) A. I. Bunea, D. Martella, S. Nocentini, C. Parmeggiani, R. Taboryski, D. S. Wiersma, *Adv. Intell. Syst.* **2021**, *3*, 2000256; c) A. Ahmadi, K. Till, Y. Hafting, M. Schüttpelz, M. Bjørås, K. Glette, J. Tørresen, A. D. Rowe, B. Dalhus, *Sci. Rep.* **2019**, *9*, 16784; d) P. N. Bernal, P. Delrot, D. Loterie, Y. Li, J. Malda, C. Moser, R. Levato, *Adv. Mater.* **2019**, *31*, 1904209. e) M. Y. Khalid, Z. U. Arif, W. Ahmed, R. Umer, A. Zolfagharian, M. Bodaghi, *Sens. Actuators, A* **2022**, *343*, 113670.

[7] a) C. A. Spiegel, M. Hippler, A. Münchinger, M. Bastmeyer, C. Barner-Kowollik, M. Wegener, E. Blasco, *Adv. Funct. Mater.* **2020**, *30*, 1907615; b) H. Y. Jeong, S.-C. An, Y. C. Jun, *Nanophotonics* **2022**, *11*, 461; c) K. Jung, N. Corrigan, M. Ciftci, J. Xu, S. E. Seo,

C. J. Hawker, C. Boyer, *Adv. Mater.* **2020**, *32*, 1903850. d) L.-Y. Hsu, C. A. Spiegel, E. Blasco, *4D Printing Principles and Fabrication, Smart Materials in Additive Manufacturing*, (Eds.: M. Bodaghi, A. Zolfagharian), Vol. *1*, Elsevier, Amsterdam, the Netherlands **2022**, pp. 231–263.

[8] a) M. Champeau, D. A. Heinze, T. N. Viana, E. R. de Souza, A. C. Chinellato, S. Titotto, *Adv. Funct. Mater.* **2020**, *30*, 1910606. b) Y. Dong, S. Wang, Y. Ke, L. Ding, X. Zeng, S. Magdassi, Y. Long, *Adv. Mater. Technol.* **2020**, *5*, 2000034.

[9] a) A. Andreu, P.-C. Su, J.-H. Kim, C. S. Ng, S. Kim, I. Kim, J. Lee, J. Noh, A. S. Subramanian, Y.-J. Yoon, *Addit. Manuf.* **2021**, *44*, 102024; b) C. A. Spiegel, M. Hackner, V. P. Bothe, J. P. Spatz, E. Blasco, *Adv. Funct. Mater.* **2022**, 2110580.

[10] S. Malekmohammadi, N. Sedghi, A. S. Aminabad, A. Zarebkohan, M. Razavi, M. Vosough, M. Bodaghi, H. Maleki, *Biomedicines* **2021**, *9*, 1537.

[11] M. del Pozo, J. A. H. P. Sol, A. P. H. J. Schenning, M. G. Debije, *Adv. Mater.* **2021**, *34*, 2104390.

[12] a) S. Nocentini, D. Martella, C. Parmeggiani, S. Zanotto, D. S. Wiersma, *Adv. Opt. Mater.* **2018**, *6*, 1800167; b) S. Nocentini, F. Riboli, M. Burresi, D. Martella, C. Parmeggiani, D. S. Wiersma, *ACS Photonics* **2018**, *5*, 3222; c) S. Woska, A. Münchinger, D. Beutel, E. Blasco, J. Hessenauer, O. Karayel, P. Rietz, S. Pfleging, R. Oberle, C. Rockstuhl, M. Wegener, H. Kalt, *Opt. Mater. Express* **2020**, *10*, 2928; d) S. Nocentini, D. Martella, C. Parmeggiani, D. S. Wiersma, *Adv. Opt. Mater.* **2019**, *7*, 1900156.

[13] a) D. Martella, D. Antonioli, S. Nocentini, D. S. Wiersma, G. Galli, M. Laus, C. Parmeggiani, *RSC Adv.* **2017**, *7*, 19940; b) H. Zeng, P. Wasylczyk, C. Parmeggiani, D. Martella, M. Burresi, D. S. Wiersma, *Adv. Mater.* **2015**, *27*, 3883; c) D. Martella, S. Nocentini, D. Nuzhdin, C. Parmeggiani, D. S. Wiersma, *Adv. Mater.* **2017**, *29*, 1704047; d) M. del Pozo, C. Delaney, M. Pilz Da Cunha, M. G. Debije, L. Florea, A. P. H. J. Schenning, *Small Struct.* **2022**, *3*, 2100158; e) M. Del Pozo, C. Delaney, C. W. M. Bastiaansen, D. Diamond, A. P. H. J. Schenning, L. Florea, *ACS Nano* **2020**, *14*, 9832; f) A. Münchinger, V. Hahn, D. Beutel, S. Woska, J. Monti, C. Rockstuhl, E. Blasco, M. Wegener, *Adv. Mater. Technol.* **2022**, *7*, 2100944; g) L. Chen, Y. Dong, C.-Y. Tang, L. Zhong, W.-C. Law, G. C. P. Tsui, Y. Yang, X. Xie, *ACS Appl. Mater. Interfaces* **2019**, *11*, 19541.

[14] M. P. D.a Cunha, M. G. Debije, A. P. H. J. Schenning, *Chem. Soc. Rev.* **2020**, *49*, 6568.

[15] Z. Huang, G. Chi-Pong Tsui, Y. Deng, C.-Y. Tang, *Nanotechnol. Rev.* **2020**, *9*, 1118.

[16] a) J. R. Hemmer, S. O. Poelma, N. Treat, Z. A. Page, N. D. Dolinski, Y. J. Diaz, W. Tomlinson, K. D. Clark, J. P. Hooper, C. Hawker, J. Read De Alaniz, *J. Am. Chem. Soc.* **2016**, *138*, 13960; b) J. R. Hemmer, Z. A. Page, K. D. Clark, F. Stricker, N. D. Dolinski, C. J. Hawker, J. Read De Alaniz, *J. Am. Chem. Soc.* **2018**, *140*, 10425; c) M. M. Lerch, W. Szymański, B. L. Feringa, *Chem. Soc. Rev.* **2018**, *47*, 1910.

[17] a) M. Lahikainen, H. Zeng, A. Priimagi, *Soft Matter* **2020**, *16*, 5951; b) M. M. Lerch, M. J. Hansen, W. A. Velema, W. Szymanski, B. L. Feringa, *Nat. Commun.* **2016**, *7*, 12054.

[18] a) H. Zeng, D. Martella, P. Wasylczyk, G. Cerretti, J.-C. G. Lavocat, C.-H. Ho, C. Parmeggiani, D. S. Wiersma, *Adv. Mater.* **2014**, *26*, 2319; b) D. Liu, D. J. Broer, *Langmuir* **2014**, *30*, 13499.

[19] Y. Zhang, W. Yang, M. Gu, Q. Wei, P. Lv, M. Li, D. Liu, W. Zhao, D. J. Broer, G. Zhou, *J. Colloid Interface Sci.* **2022**, *608*, 2290.

[20] a) A. S. Alketbi, Y. Shi, H. Li, A. Raza, T. Zhang, *Soft Matter* **2021**, *17*, 7188; b) Q. Hu, G. A. Rance, G. F. Trindade, D. Pervan, L. Jiang, A. Foerster, L. Turyanska, C. Tuck, D. J. Irvine, R. Hague, R. D. Wildman, *Addit. Manuf.* **2022**, *51*, 102575.